# Co-catalytic Effects of CoS$_2$ on the Activity of the MoS$_2$ Catalyst for Electrochemical Hydrogen Evolution

Ranjith Bose,[†,‡] Zhenyu Jin,[†] Seokhee Shin, Sungjoon Kim, Sunyoung Lee, and Yo-Sep Min*[ORCID]

Department of Chemical Engineering, Konkuk University, 120 Neungdong-Ro, Gwangjin-Gu, Seoul 143-701, Korea

S *Supporting Information*

ABSTRACT: MoS$_2$ is a promising material to replace the Pt catalyst in the electrochemical hydrogen evolution reaction (HER). It is well known that the activity of the MoS$_2$ catalyst in the HER is significantly promoted by doping cobalt atoms. Recently, the Co−Mo−S phase, in which cobalt atoms decorate the edge positions of the MoS$_2$ slabs, has been identified as a co-catalytic phase in the Co-doped MoS$_2$ (Co-MoS$_x$) with low Co content. Here, we report the effect of the incorporation of cobalt atoms in the chemical state of the Co-MoS$_x$ catalyst, which gives rise to the co-catalytic effect. Co-MoS$_x$ catalysts with various Co contents were prepared on carbon fiber paper by a simple hydrothermal process. On the Co-MoS$_x$ catalyst with high Co content (Co/Mo ≈ 2.3), a dramatically higher catalytic activity was observed compared to that for the catalyst with low Co content (Co/Mo ≈ 0.36). Furthermore, the co-catalytic phase in the Co-MoS$_x$ catalyst with the high Co content was found not to be the Co−Mo−S phase but was identified as CoS$_2$ by Raman spectroscopy, X-ray photoelectron spectroscopy, X-ray diffraction, and transmission electron microscopy. It is believed that CoS$_2$ is an alternative choice to co-catalyze HER on MoS$_2$-based catalysts.
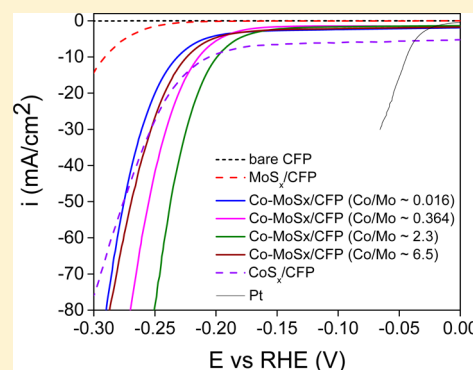
INTRODUCTION

Hydrogen gas has been considered to be a clean energy source because modern society is faced with global warming and energy shortages.[1] Electrocatalytic water splitting is one of the most effective and reliable pathways to produce hydrogen gas.[2] It is well known that platinum group metals (PGMs) are the most efficient electrocatalysts for the hydrogen evolution reaction (HER), but they are very expensive because of their small reserves. Despite in-depth studies on various HER catalysts, no catalyst ever reported has yet surpassed the performance of PGM catalysts in the large-scale production of hydrogen.[3] Thus, the development of cheap and highly active electrocatalysts is still required for the realization of the hydrogen economy.

In recent years, transition-metal dichalcogenides have been identified as a class of the most promising and attractive catalysts for electrochemical HER. MoS$_2$ is one potential alternative catalyst to replace PGMs because the Gibbs free energy of hydrogen adsorption (ΔG_{H*}) on MoS$_2$ is close to that on Pt, in addition to its abundance and low cost.[4−6] The catalytic activity of MoS$_2$ is mainly influenced by two factors. The first is the number of edge sites in MoS$_2$ because the active sites of MoS$_2$ are not the atoms in the basal plane but the sites of its edge. The second is the conductivity of MoS$_2$ because poor conductivity of the catalyst may restrict the electron transfer for the electrochemical catalysis.[7,8] Many researchers have emphasized these two issues in order to improve the HER performance of the MoS$_2$ catalyst. Many studies have focused on exposing more active edge sites to enhance the catalytic

efficiency of MoS$_2$, e.g., defect- and S-rich MoS$_2$ nanosheets,[9] edge-terminated MoS$_2$,[10] monolayer MoS$_2$ with S vacancies,[11] holey MoS$_2$ nanostructures,[12] and vertically oriented MoS$_2$.[13] Furthermore, when the MoS$_2$ catalysts are coated onto conductive matrices such as graphitic carbon nitride,[14] graphene,[4,15,16] reduced graphene oxide,[17] carbon fiber paper (CFP),[18] and gold,[19] they have shown higher HER performance. Some researchers have used a different approach in which the semiconducting 2H phase of MoS$_2$ was transformed to the metallic 1T phase to improve the electrical conductivity of MoS$_2$ and the catalytic activity.[20,21]

Among the edge sites of MoS$_2$, the Mo-edge sites are known to be more active than the S-edge sites in terms of ΔG_{H*}, even though ΔG_{H*} is influenced by the adhesion of MoS$_2$ on a support material.[22,23] There are several reports on the promotion of MoS$_2$ activity by doping transition-metal ions.[12,24−26] Chorkendorff et al. reported that the S-edge sites could become more active by incorporating cobalt because the ΔG_{H*} on the Co-doped S-edge of MoS$_2$ is very similar to that on the Mo-edge of MoS$_2$.[22] Hu's group also reported that transition-metal ions such as Fe, Co, and Ni could promote the catalytic activity of amorphous molybdenum sulfide (MoS$_x$) films that were prepared by cyclic voltammetry in an aqueous precursor solution.[24] According to a report by Norskov and Cui in which the promotional effects of Fe, Co, Ni, and Cu ions at

the S-edge sites were theoretically and experimentally investigated by using vertically aligned MoS_2 as a model catalyst, the S-edges are predicted to become similarly active with respect to the pristine Mo-edge by doping transition-metal atoms.[25] Moreover, Deng and co-workers exhibited that the catalytic activity of the in-plane S atoms in the basal plane of MoS_2 could be triggered when metal atoms (e.g., Co, Ti, Zn, Pt, and so on) substitute for the Mo atoms in the MoS_2 matrix, leaving unsaturated S atoms on the basal plane.[26]

Among the transition-metal promoters, cobalt exhibits the best promotional effect on MoS_2 catalysts.[24−26] Recently, Dai et al. reported that the Co−Mo−S phase, formed by annealing an amorphous Co-doped MoS_2 (Co-MoS_x) at a high temperature (e.g., 500 °C), plays a crucial role in the enhanced activity.[27] However, because the promotional effect of Co atoms has also been observed even in the amorphous phase of Co-MoS_2,[24,28] the origin of the promotional effect should be studied further to unveil the chemical state of the active sites.

In the study on hydrodesulfurization (HDS) catalysts based on MoS_2 with cobalt as a promoter, the Co−Mo−S phase was found and its structure was understood in atomic detail by using various spectroscopic analyses.[29] The Co−Mo−S phase, which is either active itself or at least closely associated with the active sites for the HDS reaction, is observed in Co-MoS_2 catalysts with low Co content. The Co−Mo−S phase consists of MoS_2 particles in which cobalt atoms decorate the edge positions of the MoS_2 slabs. In the report on Co-MoS_2 catalyst by Dai et al.,[27] they also prepared the Co-MoS_2 catalyst with the dominant Co−Mo−S phase, of which the Co/Mo ratio is around 0.42. However, when the catalyst has a Co/Mo ratio greater than 1, the Co−Mo−S phase may not be the dominant phase of cobalt atoms because the abundant cobalt atoms may form another phase in the Co-MoS_2 catalyst. Therefore, the incorporated number of Co atoms may be critical to the activity of the Co-MoS_2 catalyst.

Inspired by these previous reports on the Co doping of the MoS_2 catalyst, we devised a one-step hydrothermal synthesis of cobalt-incorporated molybdenum sulfide (Co-MoS_x) on carbon fiber paper (CFP) at 200 °C using an aqueous solution of molybdic acid, thioacetamide, and cobalt chloride as Mo, S, and Co precursors, respectively. Depending on the concentration of $CoCl_2$ in the aqueous precursor solution, the Co content was systematically controlled to investigate the formation of the active phase in Co-MoS_x and its effects on the HER. The Co-MoS_x on CFP exhibits remarkable HER activity, including a low Tafel slope, a large cathodic current density, and a high exchange current density, which is significantly improved compared to that of undoped MoS_x on CFP. The amount of cobalt incorporated into the MoS_x catalyst is critical to the formation of the active phase, which plays a crucial role in HER performance. As is well known, the Co−Mo−S phase is active in the Co-MoS_2 catalysts with low Co content. However, in this work, we report CoS_2 as a co-catalytic phase of the Co-MoS_2 catalysts in which the content of cobalt is much higher than that of molybdenum.

■ EXPERIMENTAL SECTION

Synthesis of Co-MoS_x/CFP. Molybdic acid (H_2MoO_4), thioacetamide (CH_3CSNH_2), and cobalt chloride ($CoCl_2$) were purchased from Sigma-Aldrich (analytical grade) and used without further purification. In a typical preparation of the precursor solution, 0.0485 g of H_2MoO_4 (0.01 M), 0.0676 g of CH_3CSNH_2 (0.03 M), and various amounts [0.0011 g (3×10^{-4} M), 0.0116 g (3×10^{-3} M), 0.1165 g (3

$\times 10^{-2}$ M), and 1.1658 g (3×10^{-1} M)] of $CoCl_2$ were weighed and dissolved in 30 mL of deionized water with vigorous stirring for 30 min. Subsequently, the resulting solutions were transferred into a Teflon-lined autoclave with a piece of carbon fiber paper (CFP) and then kept at 200 °C for 24 h in a muffle furnace. After the hydrothermal reaction, the autoclave was cooled to room temperature and the catalyst-coated CFP was obtained. The Co-MoS_x/CFP was rinsed with an adequate amount of distilled water and then dried at room temperature for a few hours. As control samples, MoS_x/CFP and CoS_2/CFP were also prepared by following similar procedures without adding $CoCl_2$ and molybdic acid, respectively.

Characterization. The composition of Co-incorporated MoS_x on CFP was analyzed by inductively coupled plasma-optical emission spectroscopy (ICP-OES, Varian 720-ES). X-ray photoelectron spectroscopic (XPS) characterization was carried out on a PHI 5000 Versaprobe (ULVAC PHI) using monochromatic Al Kα emission. Binding energies were calibrated by using the carbon 1s peak at 284.8 eV. The X-ray diffraction (XRD) patterns were measured using a Philips X'pert Pro MRD X-ray diffractometer with Cu Kα emission. Scanning electron microscope (SEM) images were obtained using a JEOL JSM-6380. For transmission electron microscopy (TEM) and energy-dispersive spectroscopic (EDS) analyses, carbon fibers with catalysts were detached from each sample, and their microstructures were imaged with a Titan TM 80-300 FEI microscope.

Electrochemical Characterization. All electrochemical measurements were performed by a typical three-electrode configuration with an electrolyte solution of 0.5 M H_2SO_4 using a Biologic (SP-150) potentiostat in which saturated Hg/Hg_2SO_4, a graphite rod, and catalyst-coated CFP (Co-MoS_x/CFP, MoS_x/CFP, and CoS_2/CFP) were used as the reference, counter, and working electrodes, respectively. Before the experiments, the geometric area of the catalyst-coated CFP was defined to be around 1 cm^2 with kapton tape. The reference electrode was calibrated with respect to the reversible hydrogen electrode (RHE) by using two Pt wires as the working and counter electrodes in 0.5 M H_2SO_4 solution while using H_2 gas to purge the solution. The electrochemical potential (E) relationship between the RHE and the electrode of Hg/Hg_2SO_4 is given by $E(RHE) = E(Hg/Hg_2SO_4) + 0.696$ V. Linear sweep voltammetry (LSV) was carried out from 0.1 to −0.3 V vs RHE to obtain a polarization curve with a scan rate of 5 mV/s. Electrochemical impedance spectroscopy (EIS) was performed to determine the series resistance of each catalyst electrode at an open circuit potential with an ac amplitude of 25 mV while scanning the frequency from 50 mHz to 200 kHz. To explain the charge-transfer resistance, EIS was also performed at an overpotential of 200 mV (vs RHE). All polarization curves were corrected for ohmic potential drop (iR) losses using the series resistance (<1.6 Ω, see Figure S1). Cyclic voltammetry (CV) measurements were performed at various scan rates (20, 40, 60, 80, and 100 mV/s) from 0.10 to 0.20 V vs RHE and were used to estimate the electrochemical double layer capacitance (C_{dl}).

■ RESULTS AND DISCUSSION

Co-incorporated MoS_x (Co-MoS_x) was directly prepared on carbon fiber paper (CFP) by using the hydrothermal reaction of molybdic acid, thioacetamide, and cobalt chloride at 200 °C for 24 h. After the hydrothermal process, the content of each element in Co-MoS_x catalysts was determined by ICP-OES as shown in Figure 1 (solid circles).

As the concentration of $CoCl_2$ in the precursor solution increases, the Co content in Co-MoS_x/CFP also increases as expected. Furthermore, both contents of Mo and S atoms also significantly vary with the concentration of $CoCl_2$, although the concentrations of Mo and S precursors are fixed to be 0.01 and 0.03 mol/L in all precursor solutions, respectively. For convenience, we denote these samples as R_1, R_2, R_3, and R_4 in which the subscript number increases with the content of Co in the Co-MoS_x catalysts, i.e., $R_1 = Mo_{0.257}Co_{0.004}S_{0.739}$, $R_2 = Mo_{0.22}Co_{0.08}S_{0.70}$, $R_3 = Mo_{0.10}Co_{0.23}S_{0.67}$, and $R_4 = $
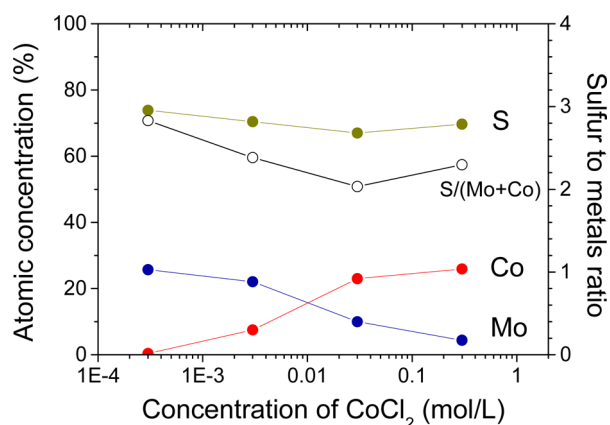
Figure 1. Atomic concentration of elements (left axis) and the anion to cation ratio (S/(Mo + Co), right axis) of Co-MoS$_x$/CFP catalysts as a function of CoCl$_2$ concentration in the precursor solution in which the concentrations of molybdic acid and thioacetamide were fixed to be 0.01 and 0.03 mol/L, respectively.

Mo$_{0.04}$Co$_{0.26}$S$_{0.70}$. By using these values, the ratios of Co/Mo are tabulated in Table 1. In addition, the loading amounts of the catalyst materials determined by ICP-OES were 33.8, 46.5, 58.1, and 48.3 μg/cm^2 for R$_1$, R$_2$, R$_3$, and R$_4$, respectively.

**Table 1. Comparison of HER Parameters of Various Co-Doped MoS$_x$ Catalysts**

samples	Co/Mo ratio	η at 10 mA/cm^2 (mV)	Tafel slope (mV/dec)	j_o (μA/cm^2)
MoS$_x$/CFP	0	291	46	0.006
R$_1$	0.016	231	60	1.31
R$_2$	0.364	214	54	1.04
R$_3$	2.3	199	51	1.28
R$_4$	6.5	224	60	1.94
CoS$_2$/CFP		100	89	44.4

The atomic ratio of sulfur to metals (S/M = S/(Mo + Co)) in the Co-MoS$_x$ catalysts is also shown in Figure 1 (open circles). In sample R$_1$, which has a small number of Co atoms, i.e., Co/Mo ≈ 0.016, the S/M ratio is around 2.83, and this value is not largely different from that (S/Mo ≈ 3) of the MoS$_x$ catalyst, which is also hydrothermally grown at 200 °C from the same Mo and S precursors, as contained in the previous report.[18] However, for sample R$_3$, the S/M ratio is around 2.03 because the content of Mo (10%) is lower than that of Co (23%).

Because of the small loading (several tens of microgram per cubic centimeter) of the catalysts, the surface morphology of the bare CFP was not significantly changed after growing MoS$_x$ or Co-MoS$_x$ on the CFP as shown in SEM images of Figure S2. It is due to the thinness of MoS$_x$ and Co-MoS$_x$ catalysts grown on CFP.[18] Considering the density (5.06 g/cm^3) of MoS$_2$, the thickness of the catalyst grown on the CFP can be roughly estimated to be several tens of nanometers. However, nanoparticles are visible in HR-TEM and scanning TEM images (Figures S3 and S4) of the Co-MoS$_x$, but any particle is not clearly detected in the MoS$_x$ catalyst. The number of nanoparticles increases as the Co content increases. Mo, Co, and S atoms are detected in several positions of the R$_3$ catalyst by TEM-EDS (Figure S4). This demonstrates that the Co atoms are well incorporated into the Co-MoS$_x$ catalyst. In addition, for the control sample of CoS$_2$/CFP, HR-TEM

images were also obtained to confirm the pyrite structure of CoS$_2$ (Figure S5). The HR-TEM and the corresponding fast Fourier transform (FFT) images (inset) clearly show the lattice fringe with an interplanar spacing of ∼0.554 nm from the (100) planes of CoS$_2$.[30]

The crystallinities of the MoS$_x$ and Co-MoS$_x$ catalysts are investigated by XRD in Figures 2a and S6. Because the CFP
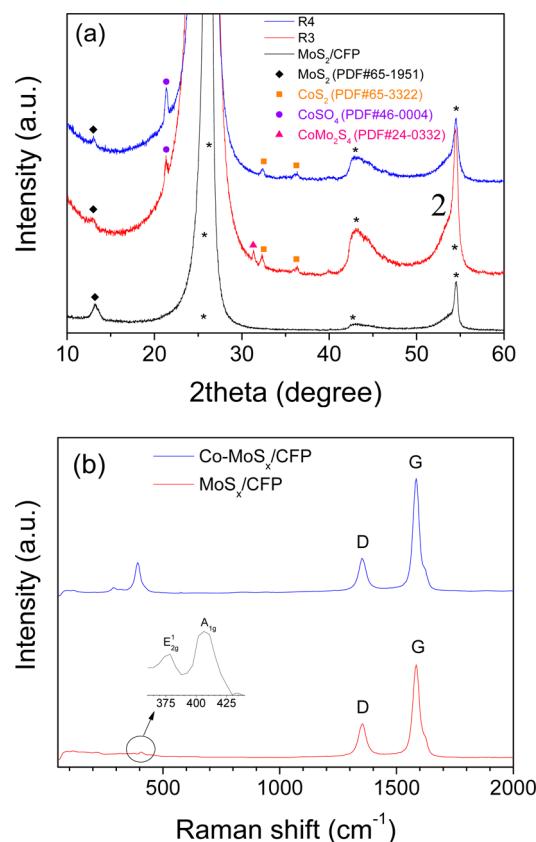
Figure 2. (a) Magnified XRD patterns of MoS$_x$/CFP and Co-MoS$_x$/CFP (R$_3$ and R$_4$) and (b) Raman spectra of MoS$_x$/CFP and Co-MoS$_x$/CFP (R$_3$). The asterisks denote XRD peaks of graphite in the bare CFP.

consists of graphitic carbons, the XRD patterns of the bare CFP, MoS$_x$/CFP, and Co-MoS$_x$/CFP (R$_3$ and R$_4$) show a strong peak at $2\theta = 26.48°$ and two weak peaks at $2\theta = 43$ and $54.54°$ from (002) and (111), (004) planes of the graphitic carbon atoms, respectively (Figure S6). Any more peaks from the catalysts are not visible without a magnification of the XRD patterns, indicating the poor crystallinity. However, after the XRD patterns are magnified (Figures 2a and S6), the characteristic peak of the basal (002) planes of MoS$_2$ is visible with a weak, broad shape at $2\theta = 13.22°$ from both MoS$_x$/CFP and Co-MoS$_x$/CFP catalysts. When Scherrer's formula is applied to the peaks, the average size of the crystallites is on the order of several tens of nanometers.[31] In addition, the interplanar spacing of the (002) planes is calculated to be around 0.669 nm. Compared to the interplanar spacing (0.615 nm) of molybdenite, this value reveals a little expansion of the (002) planes. It is well known that the interplanar spacing of the (002) planes of MoS$_2$ is generally enlarged when the size of the crystallite is on the nanoscale.[4,32,33] In addition, the incorporation of Co atoms into MoS$_2$ may also contribute to the expansion of the (002) planes in the Co-MoS$_x$ catalysts.

A weak peak that is assigned to the pyrite phase of CoS_2 is observed in the Co-MoS_x/CFP catalysts with high Co content (R_3 and R_4) in Figures 2a and S6.[34] It has already been reported that CoS_2 has higher activity than MoS_2.[30] Incidentally, a weak peak at $2\theta = 31.15°$, which can be assigned to $CoMo_2S_4$, is also observed in the R3 sample. According to a report by Sun et al.,[35] the HER activity of the $CoMo_2S_4$ phase is similar to that of the MoS_2 catalyst. Therefore, it is believed that the contribution of the $CoMo_2S_4$ phase to the HER activity of Co-MoS_x is less dominant compared to that of the CoS_2 phase in the Co-MoS_x catalyst.

A Raman spectroscopic investigation was also performed to characterize both MoS_x and Co-MoS_x/CFP catalysts. The characteristic G (1584 cm^{-1}) and D bands (1352 cm^{-1}) of graphitic carbon atoms are observed in both catalysts as a result of the presence of sp^2 carbons in the CFP. For the MoS_x/CFP catalysts, the in-plane (E^1_{2g}) and out-of-plane (A_{1g}) vibrational modes are also observed at ~379 and ~406 cm^{-1}, respectively, with a weak intensity as shown in the inset of Figure 2b. However, the Co-MoS_x/CFP catalyst with high Co content does not exhibit the corresponding peaks of E^1_{2g} and A_{1g} vibrational modes, but the two characteristic peaks of CoS_2 are significantly observed at ~290 and ~393 cm^{-1}.[28,36] Because the peak at 393 cm^{-1} is strong and broad in the range of 340 to 450 cm^{-1}, even if there are E^1_{2g} and A_{1g} peaks, they cannot be resolved in the spectral region.

XPS measurements were carried out to examine the chemical state of MoS_x/CFP and Co-MoS_x/CFP catalysts. All of the binding energies were calibrated with the carbon 1s peak at 284.8 eV. Figure 3 shows the XPS spectra of Mo 3d, S 2p, and Co 2p of MoS_x/CFP and Co-MoS_x/CFP (R_3). For the MoS_x/CFP catalyst (Figure 3a), the characteristic doublet ($3d_{3/2}$ and $3d_{5/2}$) of Mo^{4+} core electrons is observed at 232.2 and 229.0 eV, respectively, which agrees with the characteristic binding energies of the Mo^{4+} state.[5,37−40] Note that the broad peak at 226.9 eV is due to the S 2s core electrons in MoS_x.[27,41] However, the presence of a shoulder in the Mo $3d_{3/2}$ peak reveals that the chemical state of Mo^{4+} ions is mixed with that of Mo^{6+} ions.[40,41] Therefore, the Mo 3d peaks were deconvoluted by fitting the experimental data with two Mo doublets (Mo^{4+} and Mo^{6+}) and a peak of S 2s. For the deconvolution, we used two constraints: the intensity ratio (2:3) and the binding energy difference (3.13 eV) between $3d_{3/2}$ and $3d_{5/2}$ peaks. (See Table S1 for the deconvoluted binding energies of Mo 3d and S 2p.) The ratio of Mo^{6+} to Mo^{4+} is evaluated to be ~0.19 by taking a ratio of the intensities of the deconvoluted peaks.

In the sulfur spectrum of MoS_x/CFP (Figure 3b), because the doublet of S^{2-} $2p_{1/2}$ and $2p_{3/2}$ is not clearly resolved as a result of the presence of S_2^{2-} ions,[27,38,42] the S 2p spectra were also deconvoluted into two doublets under two constraints: the intensity ratio (1:2) and the binding energy difference (1.18 eV) between the $2p_{1/2}$ and $2d_{3/2}$ peaks. In general, the deconvoluted doublet of S_2^{2-} appears at a higher binding energy than that of S^{2-} (Table S1).[38] The relative ratio of S^{2-}/S_2^{2-} was determined to be ~1.92.

Compared to the MoS_x/CFP catalyst, there are significant changes in both the Mo and S spectra of Co-MoS_x/CFP (R_3) as a result of the high incorporation of cobalt ions into the MoS_x catalyst.[27,41] Four peaks are observed in the Mo 3d spectrum (Figure 3c) of Co-MoS_x/CFP, where the one at 226.9 eV corresponds to the S 2s peak and the others are attributed to an overlap of two doublets of Mo^{4+} and Mo^{6+} 3d peaks. Note
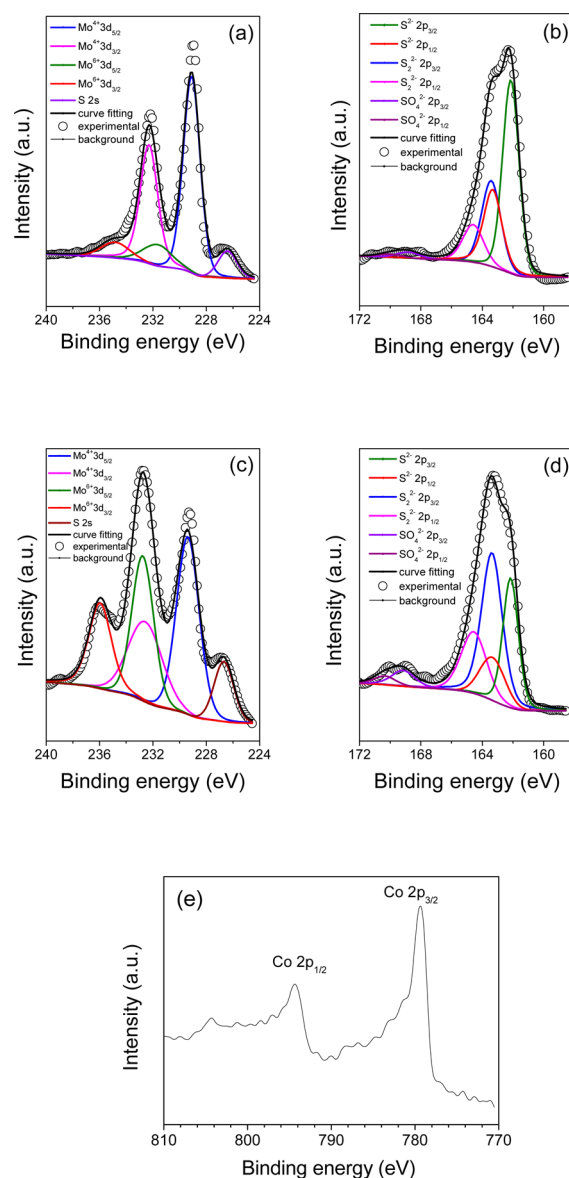
Figure 3. XPS spectra of MoS_x/CFP (a and b) and Co-MoS_x/CFP (c−e, R_3): (a, c) Mo 3d, (b, d) S 2p, and (e) Co 2p.

that the Mo^{6+}/Mo^{4+} ratio (0.77) of Co-MoS_x/CFP is much larger than the ratio (0.19) of the MoS_x/CFP catalyst (Table S1). In the S 2s spectrum (Figure 3d) of the Co-MoS_x/CFP, the contribution of the doublet of S_2^{2-} is also severe as estimated by the low S^{2-}/S_2^{2-} ratio (0.63). Such dramatic changes in the chemical states of Mo and S are related to the high incorporation of cobalt into MoS_2 (vide infra).

As identified in Figure 2, the cobalt atoms, highly incorporated into the MoS_2, exist mainly in the CoS_2 phase, which can be considered to be a pyrite (NaCl-like) structure of a cobalt atom and a sulfur atom pair (S_2^{2-}).[43] Figure 3e shows the Co 2p spectrum of Co-MoS_x/CFP (R_3). Because of the strong spin−orbit coupling (14.9 eV) of the Co 2p peak, the doublet of Co $2p_{3/2}$ and $2p_{1/2}$ appears at 779.4 and 794.3 eV, respectively, with a wide separation of 14.9 eV (Table S2). These binding energies are in good agreement with those observed in CoS_2 thin films.[36] Even though the Co_9S_8 phase may be formed by the high incorporation of cobalt, the Co_9S_8 phase is not dominantly present. According to the report of
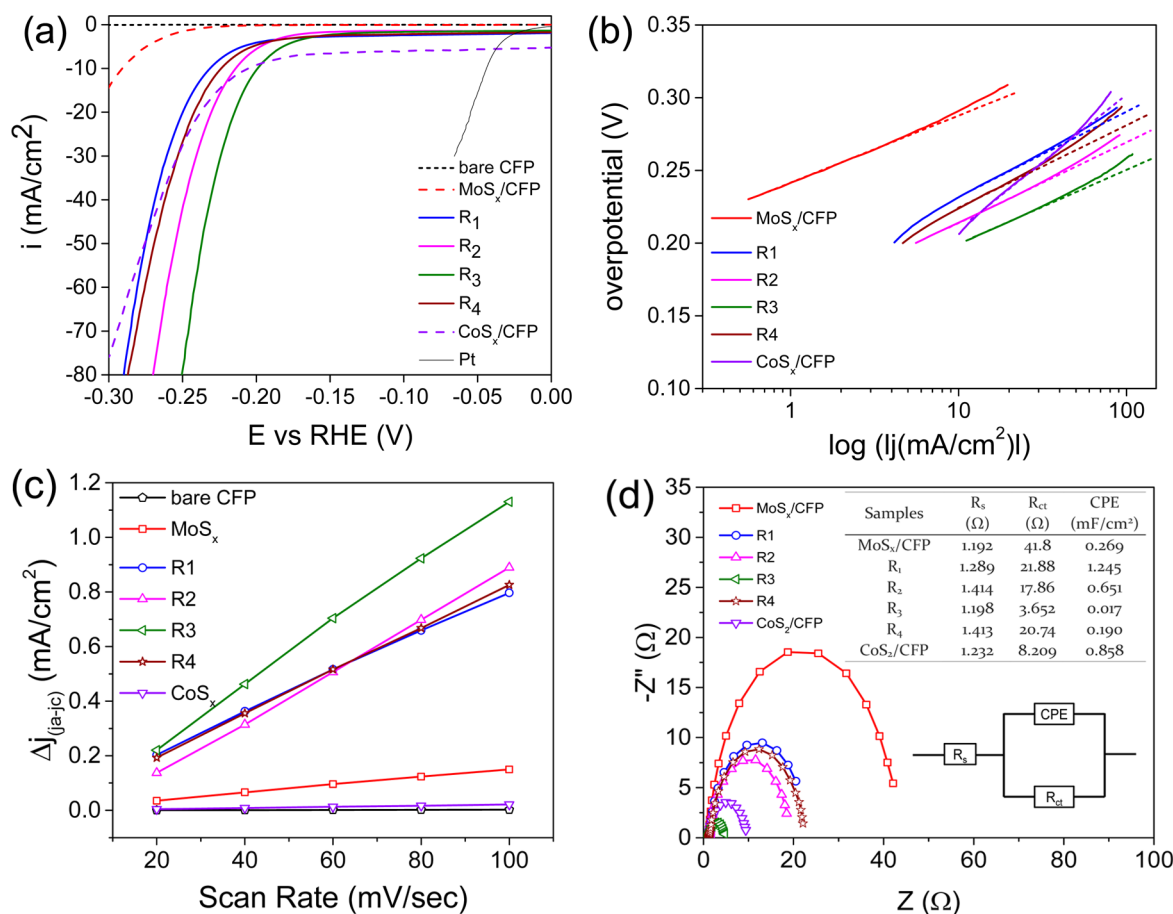
Figure 4. (a) *iR*-corrected polarization curves of MoS_x/CFP, CoS_2/CFP, and $Co\text{-}MoS_x/CFP$, (b) Tafel plots for the data presented in plot a, (c) plots showing the extraction of the double-layer capacitance (C_{dl}) for bare CFP, MoS_x/CFP, CoS_2/CFP, and various $Co\text{-}MoS_x/CFP$, and (d) Nyquist plots and fitting results (inset table) of each sample at an overpotential of 200 mV (vs RHE).

Alstrup et al., the Co $2p_{3/2}$ peak of Co_9S_8 is located at 778.4 eV, which is largely different from that (779.4 eV) of Co-MoS_x/CFP. However, because the Co 2p electrons of the Co−Mo−S phase have binding energies that are similar to those of the CoS_2 phase,[27,41,44] it is difficult to differentiate two phases by their XPS peak potions. Therefore, Alstrup et al. reported that binding energy differences were more useful for the comparison.[44] The binding energy differences, ΔE_1 and ΔE_2, are defined as $E(Co\ 2p_{3/2}) - E(S\ 2p_{3/2})$ and $E(Mo\ 3d_{5/2}) - E(S\ 2p_{3/2})$, respectively. For the Co−Mo−S phase, ΔE_1 and ΔE_2 are 617.0 and 66.9 eV, respectively. However, the Co-MoS_x/CFP (R_3) shows $\Delta E_1 = 616.0$ eV and $\Delta E_2 = 65.9$ eV, indicating that the dominant phase is not the Co−Mo−S phase but rather the CoS_2 phase, compared to the value of ΔE_1 (616.3 eV) for the CoS_2 phase (Table S3).[36]

On the other hand, SO_4^{2-} peaks are identified in the high-binding-energy region of Figure 3d ($2p_{1/2}$, 170.4 eV; $2p_{3/2}$, 169.2 eV) and Figure S7b ($2p_{1/2}$, 170.3 eV; $2p_{3/2}$, 169.1 eV), which agree with those in previous reports.[8,45] However, the S 2p spectra of SO_4^{2-} are observed only in the highly Co-doped MoS_x catalysts (R_3 and R_4), whereas there is no SO_4^{2-} peak in the MoS_x catalyst. Meanwhile, the diffraction peak (Figures 2a and S6) that is assigned to the (101) planes of $CoSO_4$ (JCPDS card no. 46-0004) is also observed at $2\theta = 21.347°$ in the XRD of the R_3 and R_4 samples. We believe that the SO_4^{2-} peak may originate from the presence of $CoSO_4$ and/or $Mo(SO_4)_3$ in which the contents increase with cobalt incorporation. Indeed,

the SO_4^{2-} peak of the R_4 catalyst is much more intense than that of the R_3 catalyst possibly because of the greater incorporation of cobalt atoms. The ratio of Mo^{6+}/Mo^{4+} also increase as more cobalt atoms are incorporated into the MoS_x catalyst (Table S1).

We evaluated the electrocatalytic HER activities of the Co-MoS_x/CFP catalysts with various Co contents using a standard three-electrode setup in a 0.5 M H_2SO_4 solution. For comparison, the catalytic activities of the bare CFP, MoS_x/CFP, and CoS_2/CFP were also estimated with the same setup. As shown in Figure 4a, bare CFP exhibits no measurable HER activity within the investigated potential range. However, the MoS_x/CFP catalyst exhibits an overpotential of 291 mV versus RHE to reach the cathodic current density of 10 mA/cm² (Table 1), which agrees with the overpotential value (290 mV) in the previous report.[18] In addition, all Co-MoS_x/CFP catalysts exhibit better HER activity with higher cathodic current densities, compared to MoS_x/CFP. However, the origins of the higher catalytic activities are different depending on the ratio of Co/Mo (Table 1). It is well known that the Co−Mo−S phase, which can be formed by decorating the edge of MoS_2 slabs with a small number of Co atoms, plays the role of promoter for the MoS_2 catalyst.[27] Owing to the Co−Mo−S phase, Co-MoS_x/CFP catalysts with low Co contents (Co/Mo < 1) exhibit higher cathodic current densities than MoS_x/CFP. In addition, their activity is improved as the Co content increases, comparing R_1 (Co/Mo = 0.016) and R_2 (Co/Mo =

0.364). This indicates that the HER activity of MoS_x on CFP has been promoted by doping cobalt atoms into MoS_x as a result of the low Gibbs free energy for hydrogen absorption (ΔG_{H*}) in the presence of the Co−Mo−S phase.[22]

However, when the Co content exceeds the Mo content (i.e., Co/Mo > 1), the cobalt atoms may not form the Co−Mo−S phase but a new phase should be formed because of the large incorporation of Co atoms. As characterized by XRD, TEM-EDS, Raman scattering, and XPS analyses for R_3 (Co/Mo ≈ 2.3) and R_4 (Co/Mo ≈ 6.5), the major phase, in which the cobalt atoms are incorporated, is identified to be the CoS_2 phase. Remarkably, the R_3 catalyst exhibits superior HER activity compared to that of other catalysts. In fact, the R_3 catalyst has achieved a geometric current density of 10 mA/cm² at only η = 199 mV (Table 1), whereas the MoS_x/CFP, R_1, and R_2 catalysts require much higher overpotentials to reach the same current density of 10 mA/cm². The overpotential for 10 mA/cm² of the R_3 catalyst is also better than those of various MoS_2-based catalysts previously reported: MoS_2 nanoparticles on carbon fiber foam (η = 210 mV),[46] MoS_x on plasma-pretreated CFP (η = 205 mV),[18] Co-doped vertically aligned MoS_2 (η = 270 mV for 2 mA/cm²),[25] V-doped MoS_2 (η = 230 mV),[47] and Se-doped MoS_2 (η = 270 mV).[48] The excellent activity of the R_3 catalyst clearly reveals that the CoS_2 phase plays the role of Co-catalyst with MoS_2 for HER. Recently, several groups have also reported the HER activity of crystalline CoS_2 of which the structure is the pyrite phase.[28,49,50] As characterized by the XRD patterns and STEM and HR-TEM images in Figures 2a, S3, and S4, the CoS_2 phase in the R_3 catalyst is also crystalline, and it shows excellent co-catalytic activity for HER. Another concern should be assigned to the R_4 catalyst. The activity of R_4 is worse than that of R_3, even though its Co/Mo ratio is 2.8 times higher than that of R_3. The degradation of the activity may be related to the formation of $CoSO_4$. which has been characterized by XRD (Figures 2a and S6) and XPS (Figure 3).

The mechanistic pathway of HER on the MoS_x and Co-MoS_x catalysts can be determined from the Tafel slope that is obtained from the slop of the linear region in a plot of overpotential (η) against logarithmic current density (log j) in Figure 4b. The Tafel slope (46 mV/dec in Table 1) of the MoS_x catalyst without Co atoms is similar to the theoretical value (40 mV/dec) of the Volmer−Heyrovsky mechanism in which a primary discharging step (Volmer reaction) for hydrogen adsorption is followed by the rate-determining step (rds) of electrochemical H_2 desorption (Heyrovsky reaction).[18] However, the Tafel slopes (50−60 mV/dec) of Co-MoS_x catalysts are slightly higher than that of the MoS_x catalyst. Previously, it was reported that a Tafel slope of 60 mV/dec reflects a chemical rearrangement step that is inserted as an rds between the Volmer and Heyrovsky steps.[51] We believe that the presence of both catalytic sites of MoS_2 and CoS_2 (or Co−Mo−S) may influence the deviation from the Tafel slopes of 40 and 60 mV/dec in the Co-MoS_x catalysts.

Another important parameter for an HER catalyst is its exchange current density (j_0), which reflects the intrinsic properties of the electrocatalyst materials. The exchange current densities of the MoS_x, CoS_2, and Co-MoS_x catalysts are listed in Table 1. The CoS_2 catalyst exhibits the most excellent exchange current density among them, even though its Tafel slope is the highest. The j_0 values of Co-MoS_x catalysts are 3 orders of magnitude greater than that of the MoS_x catalyst, owing to the formation of the co-catalytic CoS_2 phase.

The high exchange current densities clearly reveal the excellent activity of the Co-MoS_x catalysts toward the HER, and they also confirm that the incorporation of cobalt atoms into the MoS_x catalyst has decreased the absolute value of ΔG_{H*}. It should be noted that there is only a small difference in the j_0 values depending on the phase of the incorporated cobalt atoms. However, the R_3 catalyst shows the lowest series resistance (Figure S1) and charge-transfer resistance (vide infra) due to the presence of CoS_2, which is a metallic phase.[49]

The exchange current density of HER is also influenced by the electrochemically active surface area, which is commensurate with the electrical double layer capacitance (C_{dl}). As shown in Figure S8, cyclic voltammetric measurements were performed in the range of 0.10 to 0.20 V versus RHE at various scan rates (v = 20, 40, 60, 80, and 100 mV/s) because no obvious Faradaic current was observed in this range. The difference (Δj) in anodic (j_a) and cathodic (j_c) current densities, which are attributed to the capacitive charging, is plotted against the scan rate in Figure 4c. Because half of the Δj is the capacitive current density, the double-layer capacitance can be expressed as $C_{dl} = \Delta j/2v$, and the slope of each plot in Figure 4c is equal to $2C_{dl}$. As a result, the C_{dl} values of bare CFP, MoS_x/CFP, CoS_2/CFP, R_1, R_2, R_3, and R_4 are 0.01, 0.7, 0.11, 3.7, 4.7, 5.7, and 3.9 mF/cm², respectively. The C_{dl} values of all Co-MoS_x species are 1 order of magnitude greater than that of MoS_x. This indicates that the electrochemically active area increases by incorporating cobalt atoms into the MoS_x catalyst. However, this small increase in the active area cannot explain the increase of 3 orders of magnitude in the exchange current density. Therefore, we believe that the dramatic increase in j_0 by incorporating Co atoms originates from the intrinsic superior activity of Co-MoS_x/CFP by the co-catalytic effect of CoS_2 on the HER.

To investigate the charge-transfer resistance (R_{ct}) of each catalyst, the Nyquist plots of each sample were obtained in 0.5 M H_2SO_4 electrolyte at an overpotential of 200 mV (vs RHE) (Figure 4d). The inset shows an equivalent circuit model, and the EIS parameters are listed in the inset table of Figure 4d. As the Co content increases, the R_{ct} value decreases from R_1 to R_3, owing to the formation of the metallic CoS_2 phase. In particular, the R_{ct} value of the R_3 catalyst is around 3.7 Ω, which is much lower than those of both MoS_2 (~41.8 Ω) and CoS_2 (~8.2 Ω). However, the R_{ct} of the R_4 sample rather increases from that of R_3, possibly because of the formation of sulfate as characterized by XRD (Figures 2a and S6) and XPS (Figure S7).

Because the CoS_2 catalyst itself is also active in the HER (Figure 4a), the enhanced HER performance of the Co-MoS_x catalyst (R_3) can be partially ascribed to the contribution of CoS_2. However, this cannot explain why a Co-MoS_x catalyst such as R_3 exhibits much better activity than both MoS_2 and CoS_2 catalysts. If the high activity of R_3 is mainly attributed to CoS_2 itself, then the performance of R_3 cannot exceed that of the CoS_2 catalyst. Therefore, we believe that there is a synergistic effect accompanying the formation of CoS_2 in the Co-MoS_x catalyst. Even though the pyrite phase of CoS_2 exhibits metallic conductivity and a high exchange current density, its Tafel slope (89 mV/dec) is poor in the HER (vide supra). Therefore, when the Co content is adjusted to be optimal between an improvement in the exchange current density and the degradation of the Tafel slope by incorporating Co atoms, the synergistic effect of co-catalytic CoS_2 can be maximized. The comparison of the HER performance of the

Co-MoS$_x$ catalyst (R$_3$) with several previous works is listed in Table S4. Although the overpotential (199 mA/cm^2) of R$_3$ needed to reach the cathodic current density of 10 mA/cm^2 is slightly higher than those in the previous works, the small Tafel slope and the high j_0 of R$_3$ still provide another route to the formation of the co-catalytic phase of MoS$_2$ for the HER as an alternative to the Co−Mo−S phase.[24,27,28,35,52]

Finally, the stability of Co-MoS$_x$ was tested by repeating a cyclic potential scan in the range from +0.1 to −0.2 V vs RHE with a scan rate of 100 mV/s. Unfortunately, the Co-MoS$_x$/CFP catalysts show poor stability (Figure S9). The overpotential increase for R$_3$ (for a current density of 10 mA/cm^2) after the stability test of 1000 cycles is around 13 mV. However, because this value is much better than the stability of the CoS$_2$/CFP catalyst, it is expected that further study may improve the stability of the Co-MoS$_x$/CFP catalyst.

■ CONCLUSIONS

Co-incorporated MoS$_x$ catalysts were directly grown on CFP by a one-step hydrothermal method. Compared to MoS$_x$/CFP and CoS$_2$/CFP, Co-MoS$_x$/CFP exhibits more excellent electrocatalytic activity for HER. Although it is well known that the Co−Mo−S phase plays a crucial role in enhanced activity in the lightly Co-doped MoS$_x$ catalysts, the Co-MoS$_x$ catalyst with high Co content (Co/Mo > 1) has CoS$_2$ as a co-catalytic phase of cobalt atoms. Owing to the synergistic effect of metallic conductivity and the intrinsic activity of the CoS$_2$ phase, the Co-MoS$_x$ catalyst with the CoS$_2$ phase shows the best performance for HER, when the Co content is adequately controlled to an optimal amount with which the formation of sulfate ions can be inhibited.

■ ASSOCIATED CONTENT

Ⓢ Supporting Information

The Supporting Information is available free of charge on the ACS Publications website at DOI: 10.1021/acs.langmuir.7b00580.

SEM, HR-TEM, and STEM images; XRD patterns; XPS, EDS, and EIS data; and cyclic voltammograms (PDF)

■ AUTHOR INFORMATION

Corresponding Author
*E-mail: ysmin@konkuk.ac.kr.

ORCID
Yo-Sep Min: 0000-0002-2340-3633

Present Address
‡Department of Chemical Engineering, Hanyang University, 222 Wangsimni-Ro, Seongdong-Gu, Seoul 133-791, Korea.

Author Contributions
†These authors contributed equally to this work.

Notes
The authors declare no competing financial interest.

■ REFERENCES

(1) Luo, J.; Im, J.-H.; Mayer, M. T.; Schreier, M.; Nazeeruddin, M. K.; Park, N.-G.; Tilley, S. D.; Fan, H. J.; Grätzel, M. Water photolysis at 12.3% efficiency via perovskite photovoltaics and Earth-abundant catalysts. *Science* **2014**, *345* (6204), 1593−1596.

(2) Wang, M.; Chen, L.; Sun, L. Recent progress in electrochemical hydrogen production with earth-abundant metal complexes as catalysts. *Energy Environ. Sci.* **2012**, *5* (5), 6763−6778.

(3) Yin, H.; Zhao, S.; Zhao, K.; Muqsit, A.; Tang, H.; Chang, L.; Zhao, H.; Gao, Y.; Tang, Z. Ultrathin platinum nanowires grown on single-layered nickel hydroxide with high hydrogen evolution activity. *Nat. Commun.* **2015**, *6*, 6430.

(4) Li, Y.; Wang, H.; Xie, L.; Liang, Y.; Hong, G.; Dai, H. MoS$_2$ Nanoparticles Grown on Graphene: An Advanced Catalyst for the Hydrogen Evolution Reaction. *J. Am. Chem. Soc.* **2011**, *133* (19), 7296−7299.

(5) Chen, Z.; Cummins, D.; Reinecke, B. N.; Clark, E.; Sunkara, M. K.; Jaramillo, T. F. Core−shell MoO$_3$−MoS$_2$ Nanowires for Hydrogen Evolution: A Functional Design for Electrocatalytic Materials. *Nano Lett.* **2011**, *11* (10), 4168−4175.

(6) Trasatti, S. Work function, electronegativity, and electrochemical behaviour of metals. *J. Electroanal. Chem. Interfacial Electrochem.* **1971**, *33* (2), 351−378.

(7) Jaramillo, T. F.; Jørgensen, K. P.; Bonde, J.; Nielsen, J. H.; Horch, S.; Chorkendorff, I. Identification of Active Edge Sites for Electrochemical Hydrogen Evolution from MoS$_2$ nanocatalysts. *Science* **2007**, *317* (5834), 100−102.

(8) Benck, J. D.; Chen, Z.; Kuritzky, L. Y.; Forman, A. J.; Jaramillo, T. F. Amorphous Molybdenum Sulfide Catalysts for Electrochemical Hydrogen Production: Insights into the Origin of their Catalytic Activity. *ACS Catal.* **2012**, *2* (9), 1916−1923.

(9) Guo, Y.; Zhang, X.; Zhang, X.; You, T. Defect- and S-rich ultrathin MoS$_2$ nanosheet embedded N-doped carbon nanofibers for efficient hydrogen evolution. *J. Mater. Chem. A* **2015**, *3* (31), 15927−15934.

(10) Gao, M.-R.; Chan, M. K. Y.; Sun, Y. Edge-terminated molybdenum disulfide with a 9.4-Å interlayer spacing for electrochemical hydrogen production. *Nat. Commun.* **2015**, *6*, 7493.

(11) Xu, Y.; Wang, L.; Liu, X.; Zhang, S.; Liu, C.; Yan, D.; Zeng, Y.; Pei, Y.; Liu, Y.; Luo, S. Monolayer MoS$_2$ with S vacancies from interlayer spacing expanded counterparts for highly efficient electrochemical hydrogen production. *J. Mater. Chem. A* **2016**, *4*, 16524−16530.

(12) Wang, L.; Li, X.; Zhang, J.; Liu, H.; Jiang, W.; Zhao, H. One-pot synthesis of holey MoS$_2$ nanostructures as efficient electrocatalysts for hydrogen evolution. *Appl. Surf. Sci.* **2017**, *396*, 1719−1725.

(13) Yan, Y.; Xia, B.; Li, N.; Xu, Z.; Fisher, A.; Wang, X. Vertically oriented MoS$_2$ and WS$_2$ nanosheets directly grown on carbon cloth as efficient and stable 3-dimensional hydrogen-evolving cathodes. *J. Mater. Chem. A* **2015**, *3* (1), 131−135.

(14) Li, J.; Liu, E.; Ma, Y.; Hu, X.; Wan, J.; Sun, L.; Fan, J. Synthesis of MoS$_x$/g-C$_3$N$_4$ nanosheets as 2D heterojunction photocatalysts with enhanced visible light activity. *Appl. Surf. Sci.* **2016**, *364*, 694−702.

(15) Xiang, Q.; Yu, J.; Jaroniec, M. Synergetic effect of MoS$_2$ and graphene as cocatalysts for enhanced photocatalytic H$_2$ production of TiO$_2$ nanoparticles. *J. Am. Chem. Soc.* **2012**, *134*, 6575−6578.

(16) Yuan, Y.; Shen, P.; Li, Q.; Chen, G.; Zhang, H.; Zhu, L.; Zou, B.; Liu, B. Excellent photocatalytic performance of few-layer MoS$_x$/graphene hybrids. *J. Alloys Compd.* **2017**, *700*, 12−17.

(17) Zhou, J.; Xiao, H.; Zhou, B.; Hwang, F.; Zhou, S.; Xiao, W. Hierarchical MoS$_2$-rGO nanosheets with high MoS$_2$ loading with enhanced electro-catalytic performance. *Appl. Surf. Sci.* **2015**, *358*, 152−158.

(18) Bose, R.; Balasingam, S. K.; Shin, S.; Jin, Z.; Kwon, D. H.; Jun, Y.; Min, Y.-S. Importance of Hydrophilic Pretreatment in the Hydrothermal Growth of Amorphous Molybdenum Sulfide for Hydrogen Evolution Catalysis. *Langmuir* **2015**, *31* (18), 5220−5227.

(19) Shin, S.; Jin, Z.; Kwon, D. H.; Bose, R.; Min, Y.-S. High Turnover Frequency of Hydrogen Evolution Reaction on Amorphous MoS$_2$ Thin Film Directly Grown by Atomic Layer Deposition. *Langmuir* **2015**, *31* (3), 1196−1202.

(20) Lukowski, M. A.; Daniel, A. S.; Meng, F.; Forticaux, A.; Li, L.; Jin, S. Enhanced Hydrogen Evolution Catalysis from Chemically

Exfoliated Metallic MoS₂ Nanosheets. *J. Am. Chem. Soc.* **2013**, *135* (28), 10274−10277.

(21) Voiry, D.; Salehi, M.; Silva, R.; Fujita, T.; Chen, M.; Asefa, T.; Shenoy, V. B.; Eda, G.; Chhowalla, M. Conducting MoS₂ Nanosheets as Catalysts for Hydrogen Evolution Reaction. *Nano Lett.* **2013**, *13* (12), 6222−6227.

(22) Bonde, J.; Moses, P. G.; Jaramillo, T. F.; Norskov, J. K.; Chorkendorff, I. Hydrogen evolution on nano-particulate transition metal sulfides. *Faraday Discuss.* **2009**, *140*, 219−231.

(23) Tsai, C.; Abild-Pedersen, F.; Nørskov, J. K. Tuning the MoS₂ Edge-Site Activity for Hydrogen Evolution via Support Interactions. *Nano Lett.* **2014**, *14* (3), 1381−1387.

(24) Merki, D.; Vrubel, H.; Rovelli, L.; Fierro, S.; Hu, X. Fe, Co, and Ni ions promote the catalytic activity of amorphous molybdenum sulfide films for hydrogen evolution. *Chemical Science* **2012**, *3* (8), 2515−2525.

(25) Wang, H.; Tsai, C.; Kong, D.; Chan, K.; Abild-Pedersen, F.; Nørskov, J. K.; Cui, Y. Transition-metal doped edge sites in vertically aligned MoS₂ catalysts for enhanced hydrogen evolution. *Nano Res.* **2015**, *8* (2), 566−575.

(26) Deng, J.; Li, H.; Xiao, J.; Tu, Y.; Deng, D.; Yang, H.; Tian, H.; Li, J.; Ren, P.; Bao, X. Triggering the electrocatalytic hydrogen evolution activity of the inert two-dimensional MoS₂ surface via single-atom metal doping. *Energy Environ. Sci.* **2015**, *8* (5), 1594−1601.

(27) Dai, X.; Du, K.; Li, Z.; Liu, M.; Ma, Y.; Sun, H.; Zhang, X.; Yang, Y. Co-Doped MoS₂ Nanosheets with the Dominant CoMoS Phase Coated on Carbon as an Excellent Electrocatalyst for Hydrogen Evolution. *ACS Appl. Mater. Interfaces* **2015**, *7* (49), 27242−27253.

(28) Zhang, H.; Li, Y.; Xu, T.; Wang, J.; Huo, Z.; Wan, P.; Sun, X. Amorphous Co-doped MoS₂ nanosheet coated metallic CoS₂ nanocubes as an excellent electrocatalyst for hydrogen evolution. *J. Mater. Chem. A* **2015**, *3* (29), 15020−15023.

(29) Niemantsverdriet, J. W. *Spectroscopy in Catalysis: An Introduction*; VCH: Weinheim, 1995.

(30) Zhang, H.; Li, Y.; Zhang, G.; Xu, T.; Wan, P.; Sun, X. A metallic CoS₂ nanopyramid array grown on 3D carbon fiber paper as an excellent electrocatalyst for hydrogen evolution. *J. Mater. Chem. A* **2015**, *3*, 6306−6310.

(31) Cullity, B. D.; Stock, S. R. *Elements of X-ray Diffraction*, 3rd ed.; Prentice Hall: Upper Saddle River, NJ, 2001.

(32) Jin, Z.; Shin, S.; Kwon, D. H.; Han, S.-J.; Min, Y.-S. Novel chemical route for atomic layer deposition of MoS₂ thin film on SiO₂/Si substrate. *Nanoscale* **2014**, *6* (23), 14453−14458.

(33) Kwon, D. H.; Jin, Z.; Shin, S.; Lee, W.-S.; Min, Y.-S. A comprehensive study on atomic layer deposition of molybdenum sulfide for electrochemical hydrogen evolution. *Nanoscale* **2016**, *8* (13), 7180−7188.

(34) Nowack, E.; Schwarzenbach, D.; Hahn, T. Charge densities in CoS₂ and NiS₂ (pyrite structure). *Acta Crystallogr., Sect. B: Struct. Sci.* **1991**, *47* (5), 650−659.

(35) Li, Y.; Zhang, H.; Jiang, M.; Kuang, Y.; Wang, H.; Sun, X. Amorphous Co-Mo-S ultrathin films with low-temperature sulfurization as high-performance electrocatalysts for the hydrogen evolution reaction. *J. Mater. Chem. A* **2016**, *4*, 13731−13735.

(36) Zhu, L.; Susac, D.; Teo, M.; Wong, K. C.; Wong, P. C.; Parsons, R. R.; Bizzotto, D.; Mitchell, K. A. R.; Campbell, S. A. Investigation of CoS₂-based thin films as model catalysts for the oxygen reduction reaction. *J. Catal.* **2008**, *258* (1), 235−242.

(37) Merki, D.; Fierro, S.; Vrubel, H.; Hu, X. Amorphous molybdenum sulfide films as catalysts for electrochemical hydrogen production in water. *Chemical Science* **2011**, *2* (7), 1262−1267.

(38) Weber, T.; Muijsers, J. C.; Niemantsverdriet, J. W. Structure of Amorphous MoS₃. *J. Phys. Chem.* **1995**, *99* (22), 9194−9200.

(39) Yu, H.; Yu, X.; Chen, Y.; Zhang, S.; Gao, P.; Li, C. A strategy to synergistically increase the number of active edge sites and the conductivity of MoS₂ nanosheets for hydrogen evolution. *Nanoscale* **2015**, *7* (19), 8731−8738.

(40) Kibsgaard, J.; Chen, Z.; Reinecke, B. N.; Jaramillo, T. F. Engineering the surface structure of MoS₂ to preferentially expose active edge sites for electrocatalysis. *Nat. Mater.* **2012**, *11* (11), 963−969.

(41) Nikulshin, P. A.; Ishutenko, D. I.; Mozhaev, A. A.; Maslakov, K. I.; Pimerzin, A. A. Effects of composition and morphology of active phase of CoMo/Al₂O₃ catalysts prepared using Co₂Mo₁₀−heteropolyacid and chelating agents on their catalytic properties in HDS and HYD reactions. *J. Catal.* **2014**, *312*, 152−169.

(42) Muijsers, J. C.; Weber, T.; Vanhardeveld, R. M.; Zandbergen, H. W.; Niemantsverdriet, J. W. Sulfidation Study of Molybdenum Oxide Using MoO₃/SiO₂/Si(100) Model Catalysts and Mo-ᴵⱽ₃Sulfur Cluster Compounds. *J. Catal.* **1995**, *157* (2), 698−705.

(43) van der Heide, H.; Hemmel, R.; van Bruggen, C. F.; Haas, C. X-ray photoelectron spectra of 3d transition metal pyrites. *J. Solid State Chem.* **1980**, *33* (1), 17−25.

(44) Alstrup, I.; Chorkendorff, I.; Candia, R.; Clausen, B. S.; Topsøe, H. A combined X-ray photoelectron and Mössbauer emission spectroscopy study of the state of cobalt in sulfided, supported, and unsupported Co-Mo catalysts. *J. Catal.* **1982**, *77* (2), 397−409.

(45) Siriwardane, R. V.; Cook, J. M. Interactions of SO₂ with sodium deposited on CaO. *J. Colloid Interface Sci.* **1986**, *114* (2), 525−535.

(46) Guo, X.; Cao, G.-l.; Ding, F.; Li, X.; Zhen, S.; Xue, Y.-f.; Yan, Y.-m.; Liu, T.; Sun, K.-n. A bulky and flexible electrocatalyst for efficient hydrogen evolution based on the growth of MoS₂ nanoparticles on carbon nanofiber foam. *J. Mater. Chem. A* **2015**, *3* (9), 5041−5046.

(47) Sun, X.; Dai, J.; Guo, Y.; Wu, C.; Hu, F.; Zhao, J.; Zeng, X.; Xie, Y. Semimetallic molybdenum disulfide ultrathin nanosheets as an efficient electrocatalyst for hydrogen evolution. *Nanoscale* **2014**, *6* (14), 8359−8367.

(48) Ren, X.; Ma, Q.; Fan, H.; Pang, L.; Zhang, Y.; Yao, Y.; Ren, X.; Liu, S. A Se-doped MoS₂ nanosheet for improved hydrogen evolution reaction. *Chem. Commun.* **2015**, *51* (88), 15997−16000.

(49) Faber, M. S.; Dziedzic, R.; Lukowski, M. A.; Kaiser, N. S.; Ding, Q.; Jin, S. High-Performance Electrocatalysis Using Metallic Cobalt Pyrite (CoS₂) Micro- and Nanostructures. *J. Am. Chem. Soc.* **2014**, *136* (28), 10053−10061.

(50) Liu, Y.-R.; Hu, W.-H.; Li, X.; Dong, B.; Shang, X.; Han, G.-Q.; Chai, Y.-M.; Liu, Y.-Q.; Liu, C.-G. Facile one-pot synthesis of CoS₂-MoS₂/CNTs as efficient electrocatalyst for hydrogen evolution reaction. *Appl. Surf. Sci.* **2016**, *384*, 51−57.

(51) Kibsgaard, J.; Jaramillo, T. F.; Besenbacher, F. Building an appropriate active-site motif into a hydrogen-evolution catalyst with thiomolybdate [Mo₃S₁₃]²⁻ clusters. *Nat. Chem.* **2014**, *6* (3), 248−253.

(52) Liu, Y.; Shang, X.; Gao, W.; Dong, B.; Chi, J.; Li, X.; Yan, K.; Chai, Y.; Liu, Y.; Liu, C. Ternary CoS₂/MoS₂/RGO electrocatalyst with CoMoS phase for efficient hydrogen evolution. *Appl. Surf. Sci.* **2017**, *412*, 138−145.

Supporting Information

Co-catalytic effects of CoS$_2$ on activity of MoS$_2$ catalyst for electrochemical hydrogen evolution

Ranjith Bose,[†,§] Zhenyu Jin,[†] Seokhee Shin, Sungjoon Kim, Sunyoung Lee, and Yo-Sep Min[*]

Department of Chemical Engineering, Konkuk University, 120 Neungdong-Ro, Gwangjin-Gu, Seoul 143-701, Korea

[†] These authors (R.B. and Z.J.) equally contributed to this work.
[§]Current affiliation: Department of Chemical Engineering, Hanyang University, 222 Wangsimni-Ro, Seongdong-Gu, Seoul 133-791, Korea
[*] E-mail: ysmin@konkuk.ac.kr
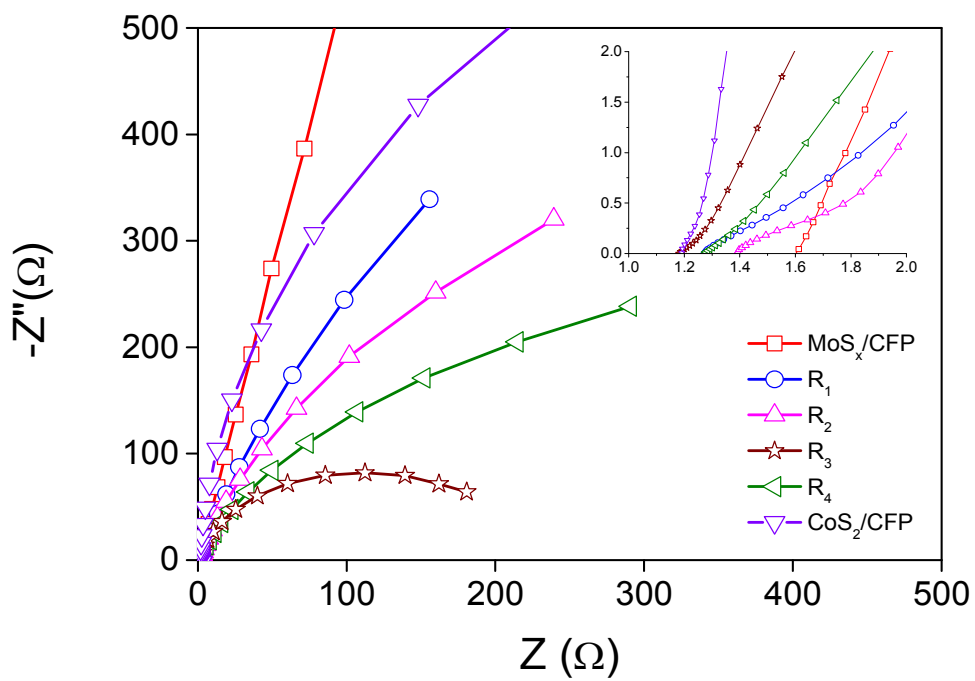
Figure S1. Nyquist plots of MoS$_x$/CFP, R$_1$, R$_2$, R$_3$, R$_4$ and CoS$_2$/CFP catalysts of which the series resistances are 1.56, 1.27, 1.39, 1.17, 1.27, and 1.19 Ω, respectively.
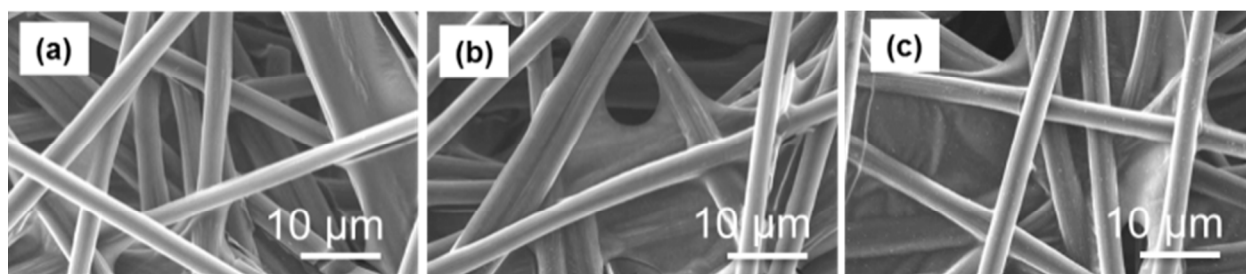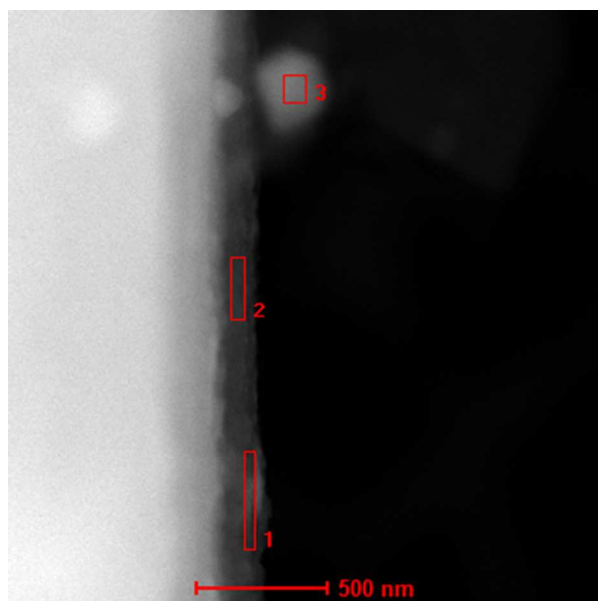
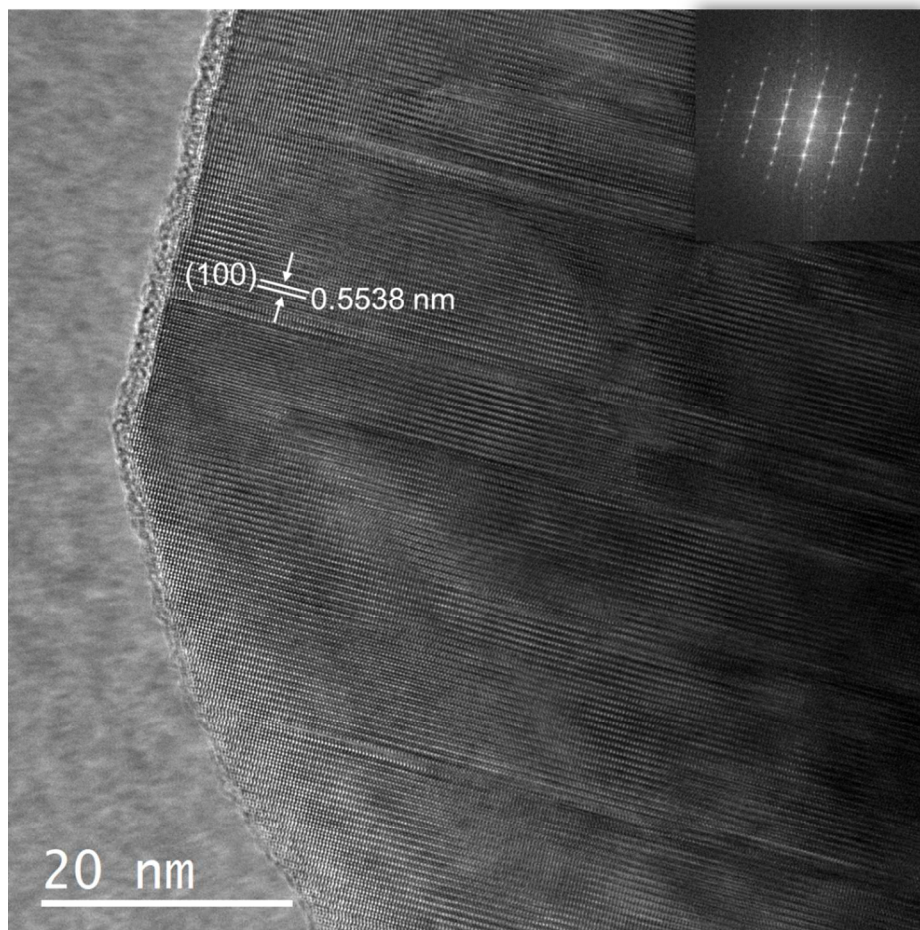**Figure S2**. SEM images of (a) bare CFP, (b) MoS$_x$/CFP, and (c) Co-MoS$_x$/CFP (R$_3$).
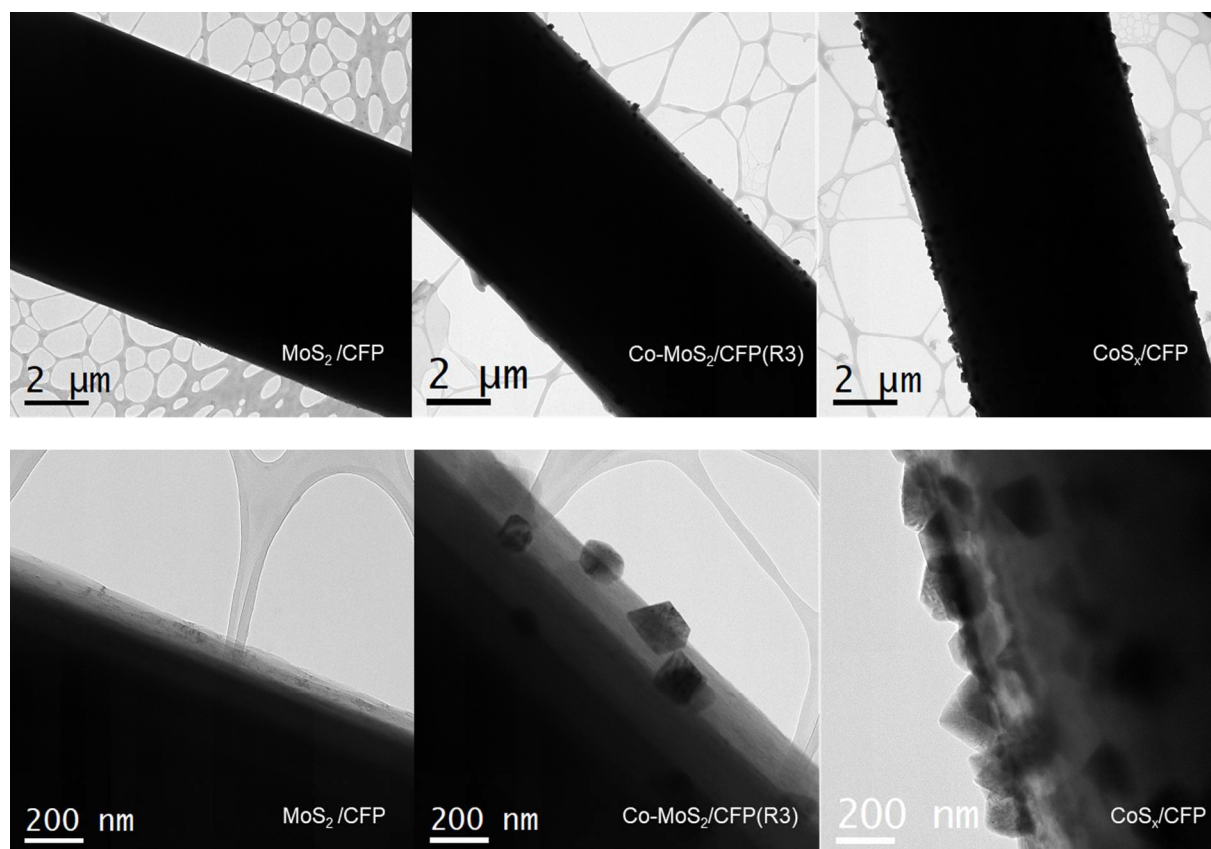
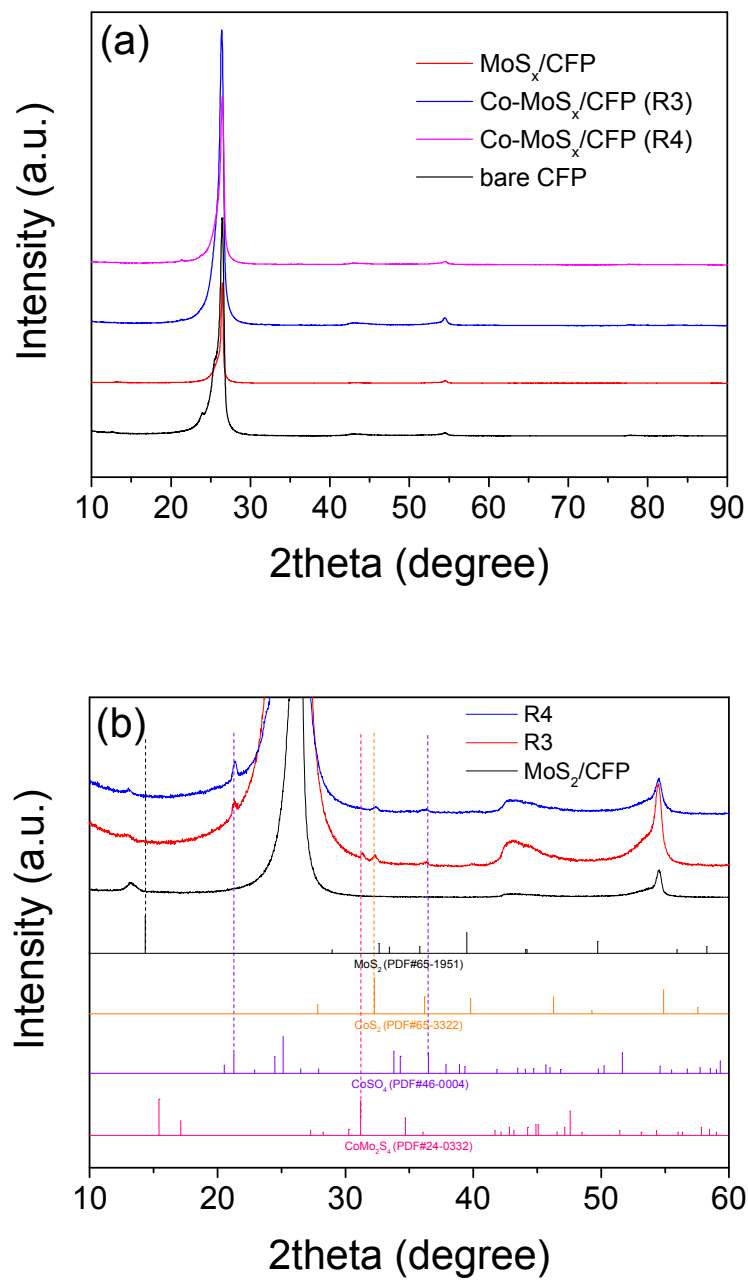**Figure S3**. HR-TEM images of MoS_x/CFP, $Co-MoS_x/CFP(R_3)$ and CoS_x/CFP.
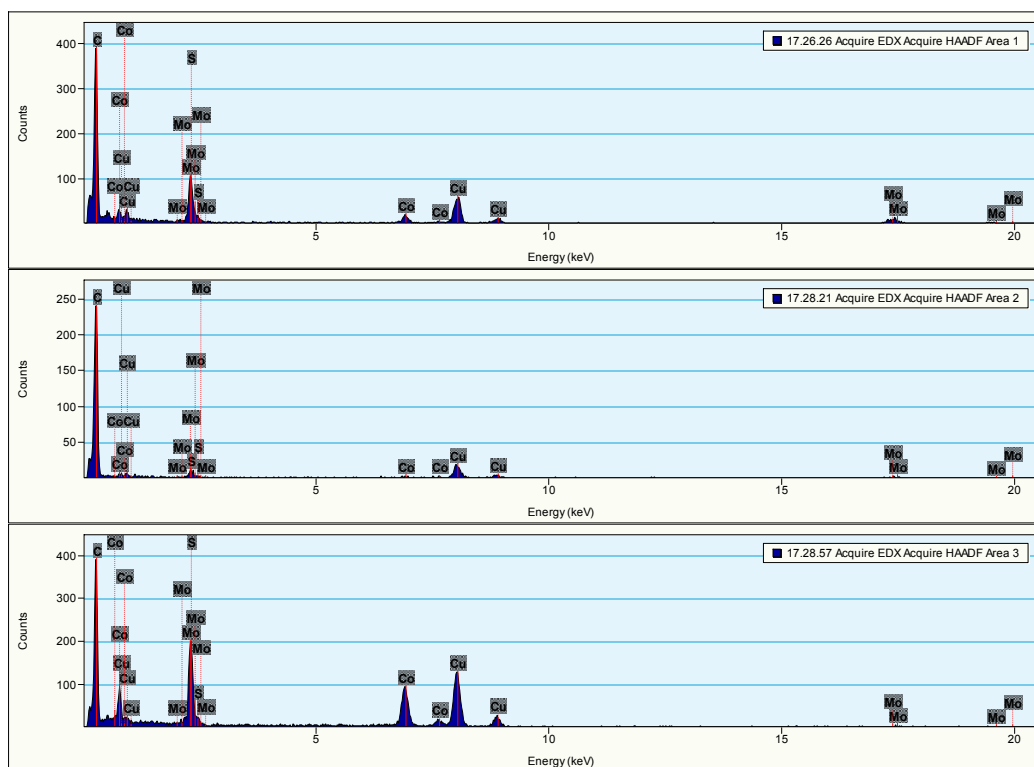
Figure S4. STEM images of R$_3$ sample (top panel) and EDS analyses (bottom panel) on different locations of R$_3$ catalyst.
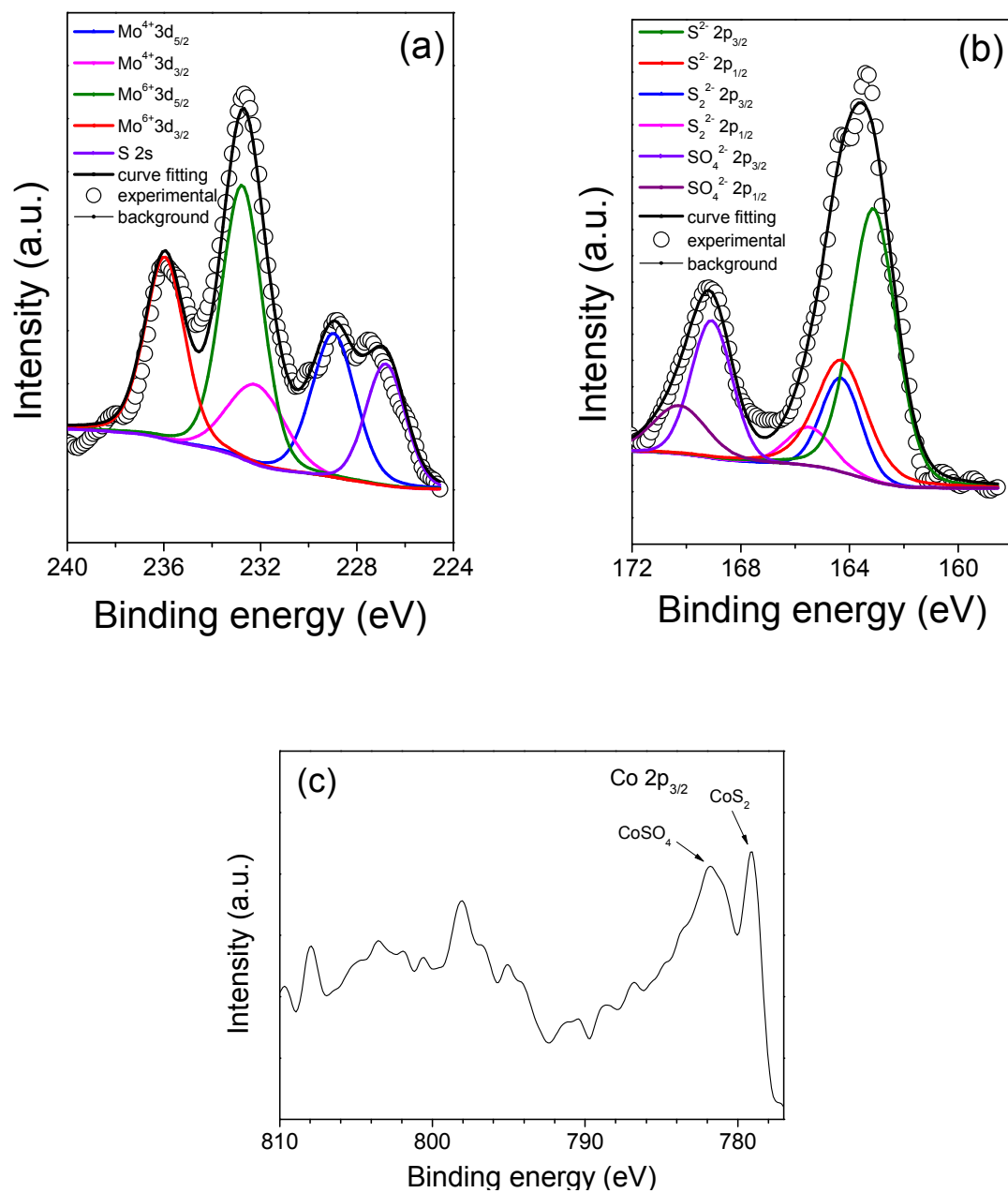
Figure S5. HR-TEM and the corresponding fast Fourier transform (FFT) images (inset) of CoS$_2$/CFP.

Figure S6. (a) XRD patterns of bare CFP, MoS_x/CFP and Co-doped MoS_x/CFP (R_3, R_4) without magnification and (b) Magnified XRD patterns of bare CFP, MoS_x/CFP and Co-doped MoS_x/CFP (R_3, R_4) with standard PDF card.

Figure S7. XPS spectra of Co-MoS$_x$/CFP (R$_4$): (a) Mo 3d, (b) S 2p, and (c) Co 2p.

Table S1. Deconvoluted XPS data for undoped and Co-doped MoS_x samples.

Samples	Mo^{4+} (eV)		Mo^{6+} (eV)		S^{2-} (eV)		S_2^{2-} (eV)		S^{2-}/S_2^{2-} ratio	Mo^{6+}/Mo^{4+} ratio
	$3d_{5/2}$	$3d_{3/2}$	$3d_{5/2}$	$3d_{3/2}$	$2p_{3/2}$	$2p_{1/2}$	$2p_{3/2}$	$2p_{1/2}$		
MoS_x/CFP	229.1	232.3	231.8	235.0	162.2	163.3	163.4	164.6	1.92	0.19
Co-MoS_x/CFP (R_3)	229.4	232.6	232.8	235.9	162.2	163.4	163.4	164.6	0.63	0.77
Co-MoS_x/CFP (R_4)	229.1	232.3	232.8	235.9	163.2	164.3	164.3	165.5	3.50	1.72

Table S2. Co 2p binding energies measured by XPS.

Samples	Co $2p_{3/2}$ (eV)		Co $2p_{1/2}$ (eV)	
	CoS_2	$CoSO_4$	CoS_2	$CoSO_4$
Co-MoS_x/CFP (R_3)	779.4	-	794.3	-
Co-MoS_x/CFP (R_4)	779.1	781.8	-	-

Table S3. Comparison of binding energy differences between R_3, CoS_2 and Co-Mo-S.

Samples	ΔE_1 (eV)[a]	ΔE_2 (eV)[a]	Ref.
Co-MoS_x/CFP (R_3)	616.0	65.9	this work
CoS_2	616.3	-	28
Co-Mo-S	617.0	66.9	36

[a] The binding energy differences ΔE_1 and ΔE_2 are defined as $\Delta E_1 = E(Co\ 2p_{3/2})-E(S\ 2p_{3/2})$ and $\Delta E_2 = E(Mo\ 3d_{5/2})-E(S\ 2p_{3/2})$, respectively.
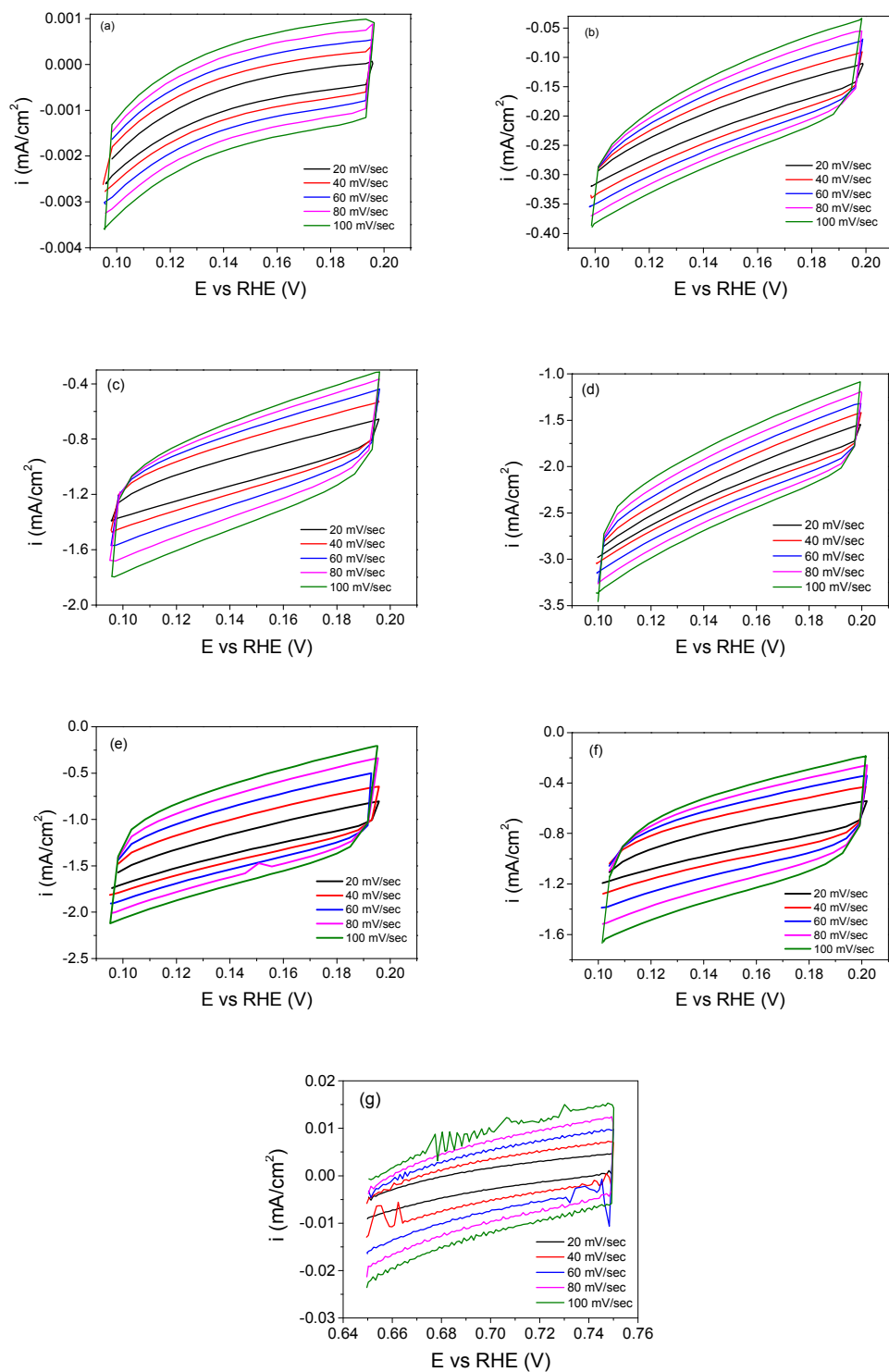
Figure S8. Electrochemical capacitance measurements for determination of surface area: (a) bare CFP, (b) MoS_x/CFP, (c) Co-MoS_x/CFP (R_1), (d) Co-MoS_x/CFP (R_2), (e) Co-MoS_x/CFP (R_3), (f) Co-MoS_x/CFP (R_4) and (g) CoS_x/CFP

10
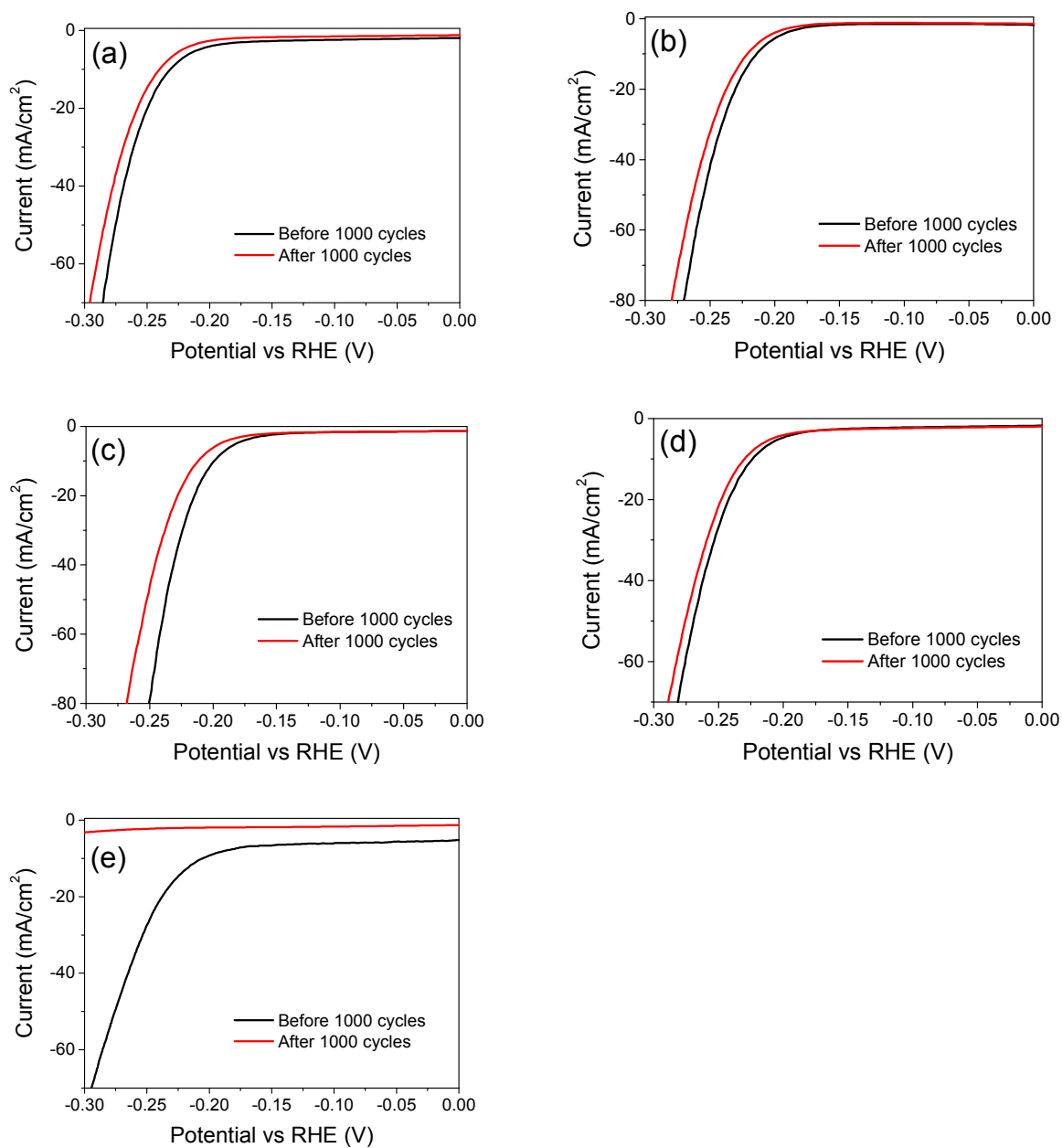
Figure S9. Stability test of each sample: (a) Co-MoS$_x$/CFP (R$_1$), (b) Co-MoS$_x$/CFP (R$_2$), (c) Co-MoS$_x$/CFP (R$_3$), (d) Co-MoS$_x$/CFP (R$_4$) and, (e) CoS$_2$/CFP.

Table S4. Comparison of HER performances of R_3 catalyst in 0.5 M H_2SO_4 electrolyte with previous works

	η at 10 mA/cm² (mV)	Tafel slope (mV/dec)	Ref.
Co-Mo-S hierachical nanosheets/Ti foil	147	54	ref. S1
CoS_2@MoS_2 nanoarray/Ti foil	111	57.3	ref. S2
Co-doped MoS_3 film/GC	188	43	ref. S3
CoS_2/MoS_2/RGO	160	56	ref. S4
CoMoS	187	38	ref. S5
Annealed CoMoS	135	50	
Co-MoS_x/CFP (R_3)	199	51	this work

S1. Li, Y.; Zhang, H.; Jiang, M.; Kuang, Y.; Wang, H; Sun, X., Amorphous Co-Mo-S ultrathin films with low-temperature sulfurization as high-performance electrocatalysts for the hydrogen evolution reaction. *Journal of Materials Chemistry A* **2016**, *4*, 13731-13735

S2. Zhang, H.; Li, Y.; Xu, T.; Wang, J.; Huo, Z.; Wan, P.; Sun, X., Amorphous Co-doped MoS_2 nanosheet coated metallic CoS_2 nanocubes as an excellent electrocatalyst for hydrogen evolution. *Journal of Materials Chemistry A* **2015,** *3* (29), 15020-15023.

S3. Merki, D.; Vrubel, H.; Rovelli, L.; Fierro, S.; Hu, X., Fe, Co, and Ni ions promote the catalytic activity of amorphous molybdenum sulfide films for hydrogen evolution. *Chemical Science* **2012,** *3* (8), 2515-2525.

S4. Liu, Y.; Shang, X.; Gao, W.; Dong, B.; Chi, J.; Li, X.; Yan, K.; Chai, Y.; Liu, Y.; Liu, C., Ternary CoS_2/MoS_2/RGO electrocatalyst with CoMoS phase for efficient hydrogen evolution. *Applied Surface Science* **2017**, *412*, 138-145

S5. Dai, X.; Du, K.; Li, Z.; Liu, M.; Ma, Y.; Sun, H.; Zhang, X.; Yang, Y., Co-Doped MoS_2 Nanosheets with the Dominant CoMoS Phase Coated on Carbon as an Excellent Electrocatalyst for Hydrogen Evolution. *ACS Applied Materials & Interfaces* **2015,** *7* (49), 27242-27253.